Chemical Engineering Journal xxx (xxxx) 176753

Contents lists available at ScienceDirect

Chemical Engineering Journal

journal homepage: www.elsevier.com/locate/cej

Engineering Li^+ solvation sheath and continuous transport pathways via weak-field ligand diluent for subzero lithium-ion batteries

Hao Huang [a], Jingang Zheng [a], Yiyang Zhao [a], Weichen Han [a], Hongyang Li [a], Lixiang Li [a], Hongwei Zhao [a], Han zhang [a], Baigang An [a], Chengguo Sun [a, b, *]

[a] School of Chemical Engineering, University of Science and Technology Liaoning, Anshan, 114051, PR China
[b] School of Chemical Engineering, Nanjing University of Science and Technology, Nanjing, Jiangsu, 210094, PR China

ARTICLE INFO

Keywords:
Weak-field ligands
Difluorobenzene
Carbonate-based electrolytes
Low temperature Li-ion batteries

ABSTRACT

Highly fluorinated diluents are widely adopted to fine-tune the solvation structure of carbonate-based electrolytes. However, their intrinsic incapability to participate in the Li^+ solvation sheath prevents establishing a continuous Li^+ transport network and impedes Li^+ rapid migration. Herein, we propose a weak-field ligand competition model to regulate the interaction between ethylene carbonate (EC) /ethyl methyl carbonate (EMC) and Li-ions. By introducing the *ortho*-difluorobenzene (DFB) into the solvation sheath, we achieve the accelerated Li^+ desolvation via DFB bidentate coordination participation in inner-sphere, and DFB also bridges adjacent solvation sheath to establish continuous ion-hopping pathways by acting as a solvation outer-sphere mediator. After applying the DFB in carbonate-based electrolyte (1 M $LiPF_6$ in EC/EMC/DFB, *v*/v/v = 3/7/10), the reconstruction of solvation sheath leads to a lower desolvation energy (2.43 eV) and higher Li^+ transport rate (3.8×10^{-7} cm^2 s^{-1}) than those with non-coordinating diluent TTE (4.35 eV and 1.4×10^{-7} cm^2 s^{-1}). Li||NCM811 cells with DFB deliver an approximately 15% higher initial discharge capacity than cells with TTE, achieving 95.7% capacity retention after 500 cycles at −20 °C, and 1.8 Ah-class graphite||NCM811 pouch cells with DFB also deliver high discharge capacity of 1.41 Ah and maintain the 94.5% capacity retention after 200 cycles at −10 °C and 0.5C.

1. Introduction

Advancing commercial carbonate-based electrolytes for high-energy-density Li-ion (Li^+) batteries with wide operating temperature ranges is urgently needed, while the poor low-temperature performance has limited their widespread application under all-weather conditions. The obstacles are primarily governed by sluggish Li^+ desolvation kinetics and organic-rich solid electrolyte interphase (SEI) [1–6]. In 1 M $LiPF_6$ in EC/EMC electrolyte, the strong-field ligands EC (C=O-Li^+ and O-Li^+) and EMC (O-Li^+) dominate the first solvation shell of Li^+, while the pristine ligand PF_6^- (F-Li^+) remains mostly free in the electrolyte. The rigid solvation structure induced by strong-field ligands exhibits kinetic inertness analogous to low-spin complexes, where Li^+ transport principally relies on the slow diffusion of the solvated entity rather than efficient ligand-exchange mechanism [7–9]. The rigid solvation structure concurrently suppresses the probability of anions entering the first solvation shell of Li^+, leading to solvent-dominated reduction reactions at the interface, which hinders the formation of a high-quality SEI rich in inorganic components (e.g., LiF) [10–17]. Therefore, fine-turning Li^+ solvation structure is the key to achieve high low-temperature performance of Li-ion batteries.

Recent advances in electrolyte-based coordination field theory involves two dominant paradigms: (1) Replacing the main solvent with a moderate donor number solvent to establish mild solvation structure. For example, both fluoroethylene carbonate (FEC) and methyl propionate (MP) instead of EC and EMC enables graphite||$LiFePO_4$ (LFP) pouch cell maintains a capacity retention of 67.7% after 100 cycles at −40 °C [18]. A series of fluorinated ethyl butyrate (EB) was introduced into carbonate-based electrolyte that allowed the 1 Ah 4.5 V graphite-based pouch cells to be cycled stably over 200 cycles at −10 °C with only a 2% capacity loss [2]. These advances have markedly enhanced the low-temperature performance of Li-ion batteries by introducing moderate donor number (DN) solvents. The solvation structures induced by median DN solvents remain predominantly solvent-separated ion pairs, in which Li^+ is strongly coordinated by solvent molecules. The strong binding energy of the C=O-Li^+ restricts rapid ligand ex-

* Corresponding author at: School of Chemical Engineering, University of Science and Technology Liaoning, Anshan, 114051, PR China.
E-mail address: sunyangguo2004@163.com (C. Sun).

https://doi.org/10.1016/j.cej.2026.176753
Received 11 March 2026; Received in revised form 19 April 2026; Accepted 25 April 2026
1385-8947/© 20XX

UNCORRECTED PROOF

Note: Low-resolution images were used to create this PDF. The original images will be used in the final composition.

change and desolvation process, thereby leading to severe polarization and capacity loss at low temperatures. (2) Promoting the entry of weakly coordinating anions into the solvation sheath by introducing diluents and more Li salts. Chen et al. reported that equal volume 1,1,2,2-Tetrafluoroethyl-2,2,3,3-tetrafluoropropylether (TTE) was added to 2 M $LiPF_6$ in DMC with lithium difluorobis(oxalato)phosphate additive allows graphite|| $LiNi_{0.6}Mn_{0.2}Co_{0.2}O_2$ pouch cell to deliver a capacity of 106 mAh g^{-1} at −20 °C [1]. Wang et al. employed 1 M LiTFSI in methyl difluoroacetate/methyl 2,2-difluoro-2(fluorosulfonyl) acetate/TTE electrolyte, which enabled graphite||$LiNi_{0.8}Mn_{0.1}Co_{0.1}O_2$ (NCM811) pouch cell to maintain 80% capacity retention after 360 cycle at −30 °C [10]. The soft solvation structure induced by anion (e.g., P-F-Li^+) coordination exhibits high kinetic activity similar to high-spin complexes in these electrolytes. The migration mode of Li^+ also shifts from diffusion transport to hopping transport, where Li^+ hop between solvents and anions by sequential shifts among various possible configurations of multidentate ligation. However, the highly-fluorinated diluents (e.g., TTE, fluorothyl, and hydrofluoroether) lack the ability to coordinate with Li^+ [1,10,19–25], merely function as inert excipients, and fail to act as Li^+ transport moieties in the electrolyte. This not only hinders the construction of a continuous Li^+ transport network but also compromises Li^+ transport kinetics. To address the issues, considerable progress has been made in establishing a continuous ion transport network with weakly coordinating diluents [26–29]. For instance, the anisole (BzO) diluent facilitates Li^+ transport by exposing ether oxygen bonds (C-O-Li^+), achieving hard-carbon||Na cells maintain high capacity and competitive cycling stability even across an extensive temperature range (−60–55 °C) [26]. Similarly, the weakly coordinating 1,3-dichloropropane diluent coordinates with Li^+ by dichloro atoms (Cl-Li^+-Cl), enabling Li ||$LiNi_{0.83}Co_{0.12}Mn_{0.05}O_2$ cells exhibit good cycling stability and high discharge capability over a wide temperature range from −60 to 60 °C [29]. However, these diluents lack sufficient stability against both high-voltage cathode oxidation and Li-metal reduction, which severely restricts their applicability in high-voltage or Li-metal battery systems.

Drawing from the above discussions, we envision a weak-field ligand diluent for Li^+ to build a soft solvation shell, which not only allows anions to enter the solvation sheath and serves as a critical bridging component for constructing a continuous Li^+ transport network, but also features high stability against high-voltage cathode oxidation and Li metal reduction. Inspired by the coordination between salicylic acid and metal ions in alkaline solution, adjacent hydroxyl and carboxyl groups on the benzene ring deprotonate and serve synergistically as bidentate ligands to form a stable five-membered chelate ring with metal ions [30–32]. We intend to exploit the ortho-coordination effect of the benzene ring for the modulation of Li^+ coordination environments. In light of the fact that ligand field intensity follows the order of $F^- < OH^- < COO^- < CN^- \approx CO$, both hydroxyl and carboxyl groups endowed with prominent coordination capability are replaced by inferior F atoms that possess relatively weaker coordination affinity. Herein, we introduced ortho-difluorobenzene (DFB) as weak-field ligand diluent to optimize a carbonate-based electrolyte (1 M $LiPF_6$ in EC/EMC/DFB, *v*/v/v = 3/7/10). The theoretical calculations and comparative experiments show that DFB can weakly coordinate with Li^+ by ortho-difluoro, resulting to form a soft solvation structure with more cation-anion aggregation. The optimized solvation structure delivers low Li^+ deslovation energy for accelerated Li^+ transports and derives superior SEI with high content of LiF. Concurrently, DFB also acts as an outer solvation structure mediator to bridge adjacent solvation clusters, establishing continuous Li^+ hopping pathways. The optimized electrolyte achieves higher ionic conductivity (1.58 mS cm^{-1} vs 1.00 mS cm^{-1} at −20 °C), Li^+ transference number (0.74 vs 0.47), and lower deslovation energy (2.43 eV vs 4.35 eV) than that of the electrolyte with TTE. Thus, the discharge specific capacity of the Li||NCM811 cells with DFB can be increased by nearly 20 mAh g^{-1} relative to TTE, the enhancement is also not available in *m*-difluorobenzene, *p*-difluorobenzene, and fluorobenzene (FB). The Li||NCM811 coin cells with DFB can achieve 95.7% capacity retention after 500 cycles at −20 °C, graphite||NCM811 pouch cells (1.8 Ah) achieve high capacity of 1.41 Ah and 94.5% capacity retention after 200 cycles at −10 °C and 0.5C.

2. Results and discussion

In 1 M $LiPF_6$ in EC/EMC electrolyte, solvents actively participate in Li^+ coordination, forming solvent dominated solvation structures, Li^+ move with their bulky solvation sheath by diffusion transport (Fig. 1a). on the contrary, after introducing highly fluorinated diluents TTE and more Li salts, the solvation structure of the electrolyte changes from solvent dominated to anion dominated. The migration mode of Li^+ shifts from diffusion transport to hopping transport, where Li^+ hop between solvents and anions by sequential shifts among various possible configurations of multidentate ligation [33,34]. However, inert diluents cannot serve as Li^+ transport sites, hindering the continuous transport of Li^+ (Fig. 1b) [34–36]. In view of the above discussion, we now introduce a weak-field ligand diluent DFB. It not only maintains the anion dominated solvation structure of the electrolyte, but also serves as a transport site for Li^+, leading to continuous hopping transport of Li^+ (Fig. 1c). To further evaluate the ligand field intensity of 11 diluents for Li^+, the electrostatic potential had been used to quantify the solvation ability of solvent molecule and elucidate the interaction between Li^+ and solvents in electrolytes [37–39]. The weak lowest negative electrostatic potential (ESP_{min}) and strong highest positive electrostatic potential (ESP_{max}) are the main characteristics of non-coordinated diluents. As shown in Fig. 1d and S1, it can be found that the DFB, Furan, FB, and benzene (Ph) have the higher absolute value of ESP_{min} than that of their ESP_{max} within the 11 diluents, indicating that they have a stronger coordination affinity with Li^+ than others. The highest occupied molecular orbital (HOMO) energy level also demonstrates the lower value of DFB, FB, Ph than that of Furan, suggesting DFB, FB, and Ph feature higher high-voltage stability than that of Furan (> 4.2 V, Figs. 1e and S2) [40,41]. However, due to the absence of fluorine substituents on the benzene ring, the Ph exhibits the serious immiscibility with carbonate-based electrolyte (Fig. S3). Therefore, we preliminarily considered DFB and FB as candidate for high-voltage weak-field ligand diluents, and non-coordinated TTE acts as a control sample.

Fig. 2a shows the electrochemical performances of three diluents used in Li||NCM811 cells. At 25 °C and 3C, the Li||NCM811 cells with 1 M $LiPF_6$ in EC/EMC/DFB (BE-DFB), EC/EMC/FB (BE-FB), and EC/EMC/TTE (BE-TTE) deliver the initial discharge capacity of 176.7, 154.3, and 154 mAh g^{-1}, respectively. The DFB has the maximum impact on the capacity performance of cell, implying that DFB as weak-field ligand contributes to the electrolyte solvation structure and ion transport kinetics. We also suspect that there is a specific reason why FB fails to enhance the initial discharge capacity. In light of the influence of adjacent difluoro atoms, both *m*-difluorobenzene and *p*-difluorobenzene were used to the aforementioned same experiments, their initial discharge capacities were 154.9 mAh g^{-1} for *m*-difluorobenzene and 153.5 mAh g^{-1} for *p*-difluorobenzene, which are similar to the function of FB (Fig. S4). The results indicate that the adjacent difluoro substituents can participate in the coordination with Li^+ and regulate the solvation structure. To further prove this hypothesis, we replaced one of the ortho-fluorine atoms of DFB with a methoxy group or trifluoromethoxy group to obtain high coordination ability with Li^+ (Fig. S5). Both 2-fluoroanisole (FBzO) and 2-(trifluoromethoxy) fluorobenzene (TFBzO) were introduced to electrolyte, the Li||LFP cells with 1 M $LiPF_6$ in EC/EMC/FBzO and Li||NCM811 cells with EC/EMC/TFBzO deliver the initial discharge capacity of 127 and 170 mAh g^{-1}, respectively (Fig. S6 and S7). The FBzO and TFBzO have the same functionalities as the DFB, demonstrating the

UNCORRECTED PROOF

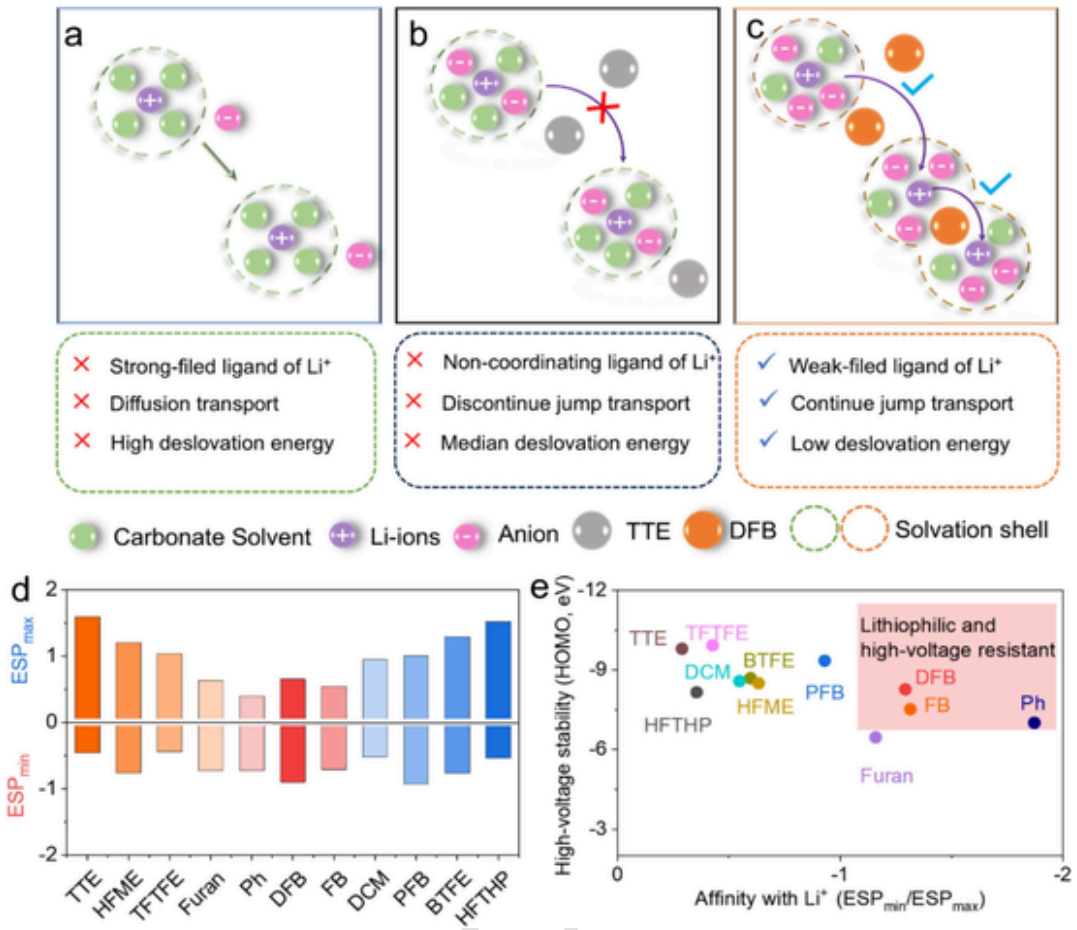

Fig. 1. (a) The schematic illustration of Li^+ transport in BE electrolyte. (b) The schematic illustration of Li^+ transport in BE-TTE electrolyte. (c) The schematic illustration of Li^+ transport in BE-DFB electrolyte. (d) The ESP_{min} and ESP_{max} of diluents. (e) The HOMO energy level and ESP_{min}/ESP_{max} of diluents.

adjacent difluoro atoms contribute to the formation of Li^+ solvation structures in electrolyte. As shown in Fig. 2c and S8, fro atoms, facilitating the formation of a five-membered coordination structure, which is confirmed by the binding energy between Li^+ and the diluents (Fig. 2d), the ortho F atoms of DFB coordinate with Li^+ exhibit the lower binding energy (−1.72 eV) than that of TTE (−1.24 eV) and FB (−1.01 eV). To illustrate the coordination behavior between diluents (TTE, FB, and DFB) and Li^+, the ^{19}F nuclear magnetic resonance (NMR) was used to examine the electrolytes (Fig. 2b). After dissolving the $LiPF_6$ in the EC/EMC/TTE and EC/EMC/FB solvents, the peaks of F atoms show negligible changes in the chemical shifts. The F atom on FB was about 0.02 ppm, and the F atoms at different position on TTE were 0.04, 0.07, 0 and 0 ppm, respectively. In contrast, an obvious shift of 0.30 ppm was observed for the F atoms in DFB, indicating a moderate interaction forces between the F atoms and Li^+ (Fig. S9) [42,43]. In addition, the UV spectrum of BE-DFB shows a significant red shift compare with pure DFB, with the content of DFB increases, the UV spectrum gradually shifts blue and returns to the initial position of pure DFB, indicating that the surplus DFB can serve as an outer-sphere medium to establish a continuous Li^+ hopping pathway (Fig. S10). The Fourier transform infrared spectrometer reveals that the peak of C—F in DFB shifts from 1266 to 1260 cm^{-1} after dissolving $LiPF_6$, these results further suggest a coordinating interaction between the adjacent F atoms with Li^+ (Fig. S11). Fig. 2e shows that the ^7Li NMR spectra of BE-DFB and BE-TTE, the chemical shift of Li^+ is −0.45 ppm for BE-DFB, −0.58 ppm for BE-TTE, which manifests that DFB participating in Li^+ coordination leads to significant changes in the chemical environment of Li^+ in electrolyte [44]. Figs. 2f and S12 compare the ionic conductivities of BE-DFB and TTE over the −20 to 40 °C range. The ionic conductivities of BE-DFB are 7.54, 6.22, 2.46, and 1.58 mS cm^{-1} at 40, 25, −10, −20 °C, respectively, which are increased by 24.4–58.0% as compared with that of the BE-TTE. Fig. 2g shows that the Li^+ transport number of BE-DFB is 0.74, which is almost 1.6 times higher than that of BE-TTE (0.47, Fig. S13). The results indicate that DFB with ortho-effects as a weak-field ligand diluent can effectively enhance the transport kinetics of Li^+.

To validate the existence of DFB coordinate with Li^+, the molecular dynamics simulation was used to investigate the Li^+ coordination in BE-TTE and BE-DFB. It can be found that each Li^+ in BE-DFB is coordinated by 0.70 EMC, 0.84 EC, 2.13 PF_6^-, and 0.15 DFB, the corresponding peaks of Li-O(EC), Li-O(EMC), Li-F(PF_6^-), Li-F(DFB) at 1.96, 1.95, 1.88 and 2.01 Å, respectively (Fig. S14 and 3b). In contrast, the coordination numbers of Li^+ in BE-TTE. with EMC, EC, PF_6^-, and TTE are 0.53, 0.99, 1.82, and 0, respectively, the corresponding peaks at 1.94, 1.93, and 1.86 Å (Fig. S15 and 3e). Based on the definition of the first solvation sheath (< 3 Å), the solvent molecules (EMC, EC, and DFB) except for TTE are located in the first solvation sheath area (< 3 Å). Unlike EMC and EC, DFB molecules are aggregated on the outer layer of the solvated shell. The results indicate that the introduction of DFB expands the solvation shell of Li^+ with EC, EMC, and PF_6^-, thus facilitating the participation of more anions in coordination. Fig. 3c further summarizes the effect of DFB on Li^+-anion aggregates. In the BE-DFB, the contents of Li^+-2PF_6^--solvents and Li^+-2PF_6^--solvents are 40.33% and 12.5%, respectively, which are higher than that of TTE (34.84%

UNCORRECTED

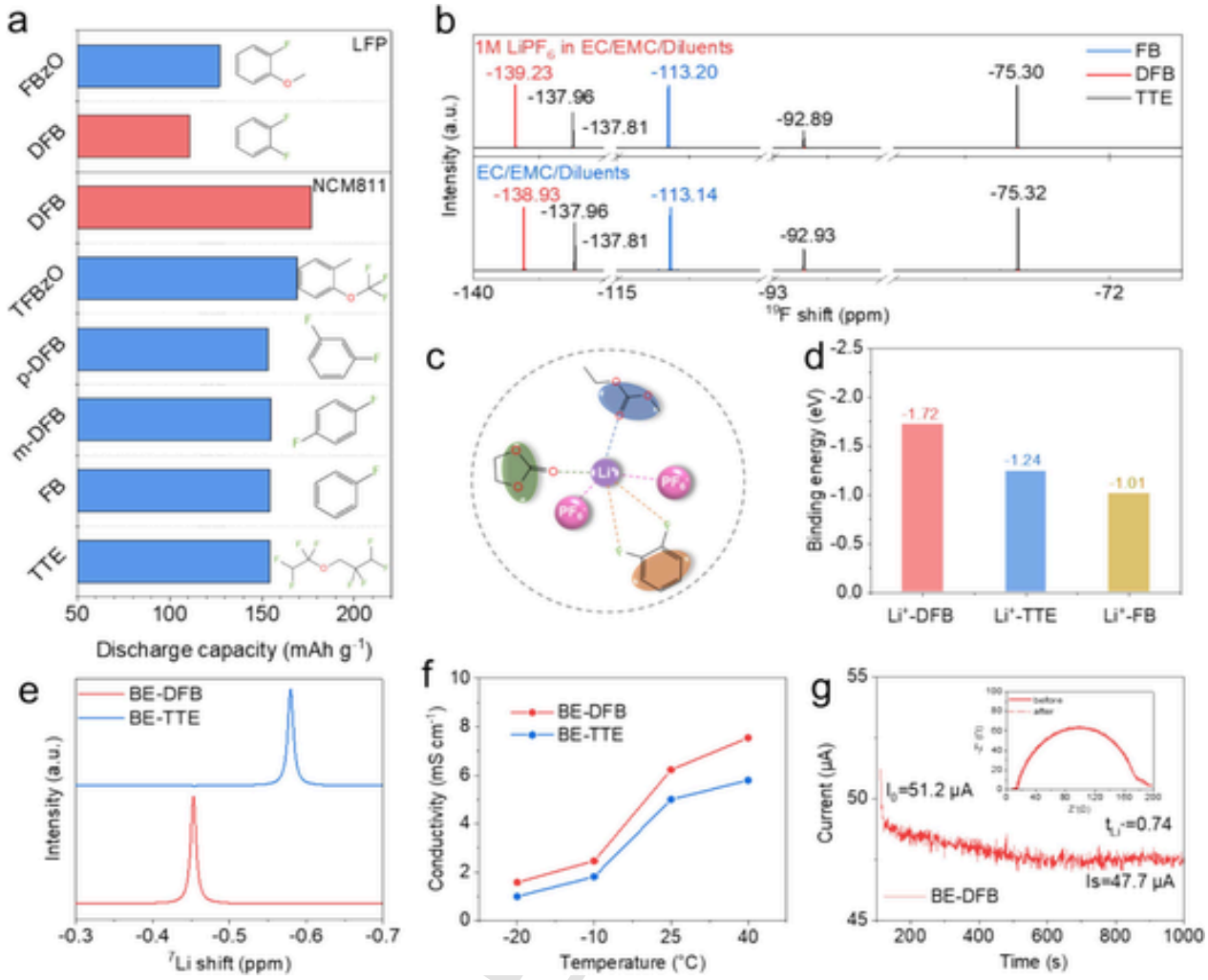

Fig. 2. (a) The electrochemical performance of Li||NCM811 and Li||LFP cells using different diluents. (b) The ^{19}F NMR spectra of EC/EMC/TTE, EC/EMC/DFB, EC/EMC/FB mixed solvents, and BE-TTE, BE-DFB, BE-FB electrolytes. (c) The solvation structure of BE-DFB. (d) The binding energies of Li^+ with DFB, TTE, and FB. (e) The ^7Li NMR spectra of BE-TTE and BE-DFB. (f) The ionic conductivities of BE-TTE and BE-DFB at different temperature. (g) The Li^+ transport number of BE-DFB.

and 7.2%). The results highlight that the coordination of lithiophilic groups (adjacent difluoro atoms) in DFB can induce spatial confinement effects, thereby promoting the formation of anion-Li^+ aggregates. Further evidence can be found from the Raman spectra. The peak of P—F stretching vibration exhibits a blue shift in BE-DFB compare to BE-TTE (Fig. 3f) [45]. As shown in Fig. 3a and d, depictions of typical solvation structures for BE-DFB and BE-TTE were obtained from molecular dynamics simulations, density functional theory calculations reveal that the desolvation energy of BE-DFB is 2.43 eV, which is much smaller than that of BE-TTE (4.35 eV). Similarly, Li^+ diffusivity was also obtained from the mean squared displacement of molecular dynamics simulations (Fig. 3g). The Li^+ diffusivity of BE-DFB was calculated to be 3.8×10^{-7} cm^2 s^{-1}, which is 2.7 times that of BE-TTE (1.4×10^{-7} cm^2 s^{-1}). Benefiting from the high Li^+ diffusivity in BE-DFB, the transport distance of Li^+ in BE-DFB is 0.14 nm, whereas that in BE-TTE is only 0.08 nm (Fig. S16). Considering that the introduction of DFB into carbonate-based electrolytes enables low desolvation energy and high Li^+ diffusion, we concluded that DFB can promote the Li^+ transport kinetics in electrolyte. To further investigate the desolvation barrier of Li^+ at the SEI film, Tafel plot analysis was conducted. The exchange current density for Li||BE-DFB||Li cells is 0.066 mA cm^{-2}, much higher than that of Li||BE-TTE||Li cells (0.050 mA cm^{-2}, Fig. 3h). Electrochemical impedance spectroscopy was also used to evaluate the desolvation barrier of Li^+ at the SEI. The Li||Li cells with BE-DFB and BE-TTE were cycled 10 times to ensure the complete formation of the SEI film before testing. The cycled Li||BE-DFB||Li cells exhibited lower interfacial resistance than that of Li||BE-TTE||Li cells at different test temperature (Fig. S17). It is worth mentioning that the interface activation energy of BE-DFB was calculated to be 57.5 kJ mol^{-1} via Arrhenius equation, which is smaller than that of BE-TTE (64.2 kJ mol^{-1}, Fig. 3i). These results indicate that the introduction of weak-field ligand DFB into carbonate-based electrolytes enables the construction of a SEI film with low Li^+ transport energy barriers, effectively facilitating the desolvation kinetics at the interface.

To investigate the interface compatibility between the electrolyte and Li metal anode, Li||Li symmetric cells were used to explore the Li plating/stripping reversibility. As shown in Fig. 4a, at a current density from 0.1 to 3 mA cm^{-2}, Li||Li cells with BE-DFB have smaller overpotentials than those cells with BE-TTE. Moreover, Li||BE-DFB||Li symmetric cells perform normally at 3 mA cm^{-2}, while the Li||BE-DFB||Li cells appear short circuited spot (Fig. S18). After long cycling at 1 mA cm^{-2} (Fig. 4b), Li||Li cells with BE-DFB have a stable cycling performance for 320 h, while the obvious short circuit was observed for Li||BE-TTE||Li cells after only 180 h. To further prove the high compatibility of BE-DFB with Li anode, the Coulombic efficiency was evaluated by stringent Li—Cu Aurbach testing. The calculated average Coulom-

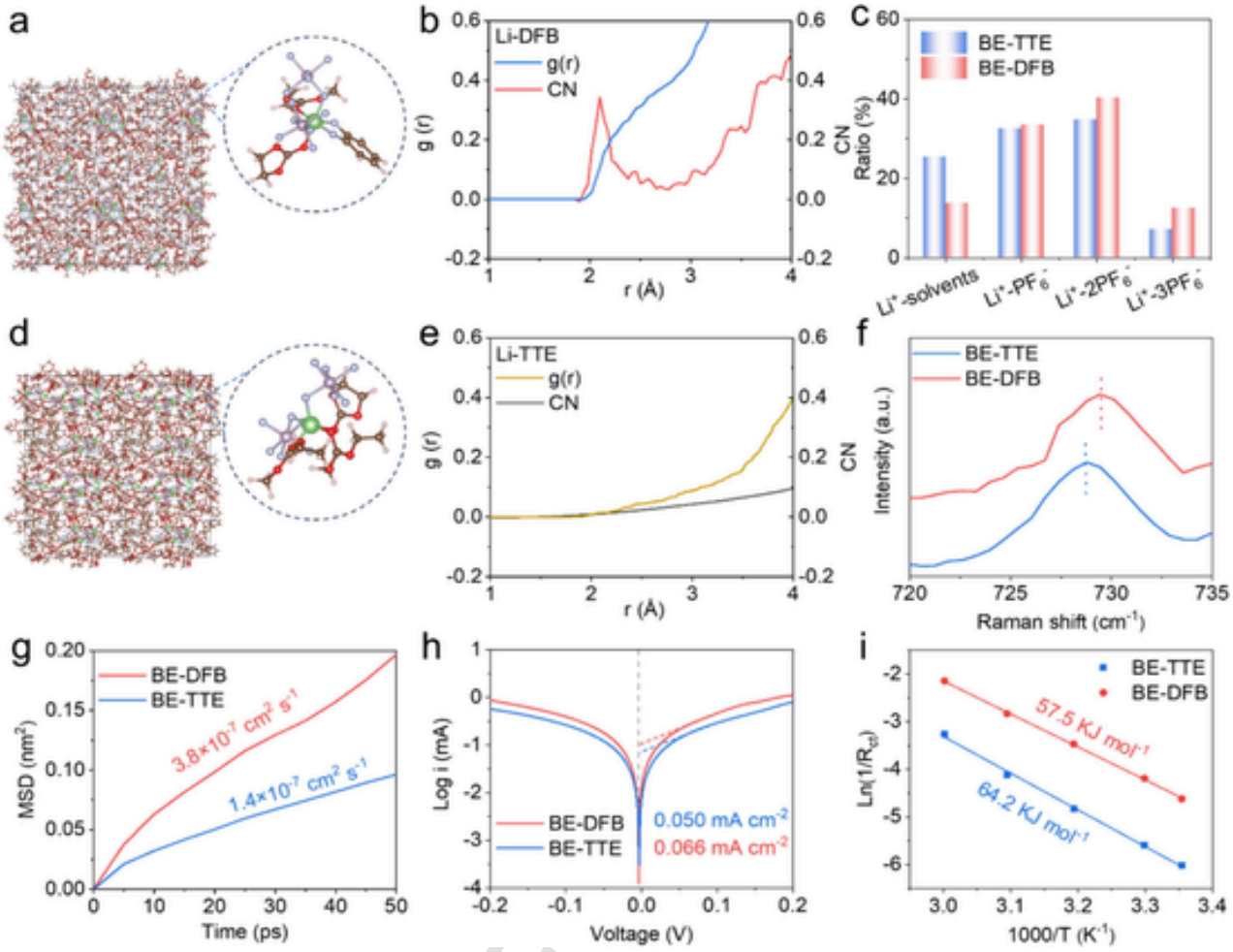

Fig. 3. (a) The molecular dynamic simulation snapshot and typical solvation structure of BE-DFB. (b) The radial distribution function of DFB in BE-DFB. (c) Composition distributions in the Li^+ primary solvation sheath in BE-TTE and BE-DFB. (d) The molecular dynamic simulation snapshot and typical solvation structure of BE-TTE. (e) The radial distribution function of TTE in BE-TTE. (f) The Raman spectra of BE-DFB and BE-TTE. (g) Mean square displacement and Li^+ diffusion coefficient in BE-TTE and BE-DFB. (h) Tafel plots of Li||Li cells using different electrolytes. (i) Arrhenius plots and activation energies for Li^+ desolvation at different temperature.

bic efficiencies of Li||BE-DFB||Cu and Li||BE-TTE||Cu are 98.3% and 91.3%, respectively (Fig. 4c). After long cycling for 200 cycles, the Li||Cu cells with BE-DFB also exhibit high stability with 95.41% average Coulombic efficiency, which is much higher than that of Li||BE-TTE||Cu cells after 52 cycles (64.23%, Fig. 4d). The superior deposition/stripping behavior of Li metal is attributed to the low nucleation overpotential of Li||Cu cells with BE-DFB (237 mV). In contrast, the high nucleation overpotential of Li||Cu cells with BE-TTE (401 mV) results in the loss of active Li (Fig. 4e) [46]. Scanning electron microscopy (SEM) was used to visualize the morphology of Li deposition on the Cu foil. After depositing an equal capacity (5 mAh), the Li metal deposited on Cu foil with BE-TTE electrolyte exhibits loose and uneven block like morphology (Fig. 4f), while the Li metal deposited using BE-DFB electrolyte exhibits a uniform and compact surface (Fig. 4g). The cross-section SEM images reveal that the thickness of Li-metal deposited using BE-DFB is 10.4 μm (Fig. 4h), which is much thinner than that of those using BE-TTE (17.5 μm, Fig. 4i). At low-temperature of −20 °C, the CE_{avg} of Li|| BE-DFB ||Cu is 92.8% during the 100 cycles at 0.5 mA cm^{-2} (Fig. S19), and the Li-symmetric cells can achieve 200 h of long-term cyclic stability at 0.5 mA cm^{-2}. (Fig. S20). In addition, the interface resistance of the cycled Li||Li cell with BE-DFB is 856 Ω, which is much smaller than that of BE-TTE (1589 Ω, Fig. S21). These results demonstrate that the SEI derived from BE-DFB electrolyte can effectively improve Li metal deposition and stripping, suggesting its potential for enabling high-performance Li metal batteries.

To evaluate the electrochemical performance, the Li||NCM811 coin cells were assembled with BE-TTE and BE-DFB electrolytes tested at 25 °C and 0.2C. The Li||NCM811 cells with BE-DFB delivered a higher initial discharge specific capacity (205.3 mAh g^{-1}) than that of those using BE-TTE (185.2 mAh g^{-1}, Fig. 5a). At different C-rates, the Li||BE-DFB||NCM811 cells deliver the discharge specific capacities of 186.5, 175.1, 166.4, 157.4, and 148.5 mAh g^{-1} at 1, 2, 3, 4, and 5C, respectively, which are much higher than that of Li||NCM811 cells using BE-TTE (Fig. 5b and S22). Regarding the long-term cycling performance, the Li||BE-DFB||NCM811 cells demonstrate superior long-term cycling stability with a capacity retention of 96.6% versus 88.9% for Li||BE-TTE||NCM811after 200 cycles. At 60 °C and 3C, the Li||NCN811 cells using BE-DFB deliver the initial discharge capacity of 194.1 mAh g^{-1} and 86.6% capacity retention after 200 cycles (Fig. S23). Even at low temperature of −20 °C, the Li||NCM811 cells with BE-TTE and BE-DFB electrolytes exhibit initial discharge specific capacity of 166.6 and 144.2 mAh g^{-1} at 0.1C, respectively (Fig. 5d). After increasing the charging and discharging rate to 0.2C, the Li||NCM811 cells with BE-DFB achieve the first discharge specific capacity of 145 mAh g^{-1} and 95.7% capacity retention after 500 cycles, while the Li||NCM811 cells with BE-TTE only achieve the first discharge specific capacity of 126

UNCORRECTED

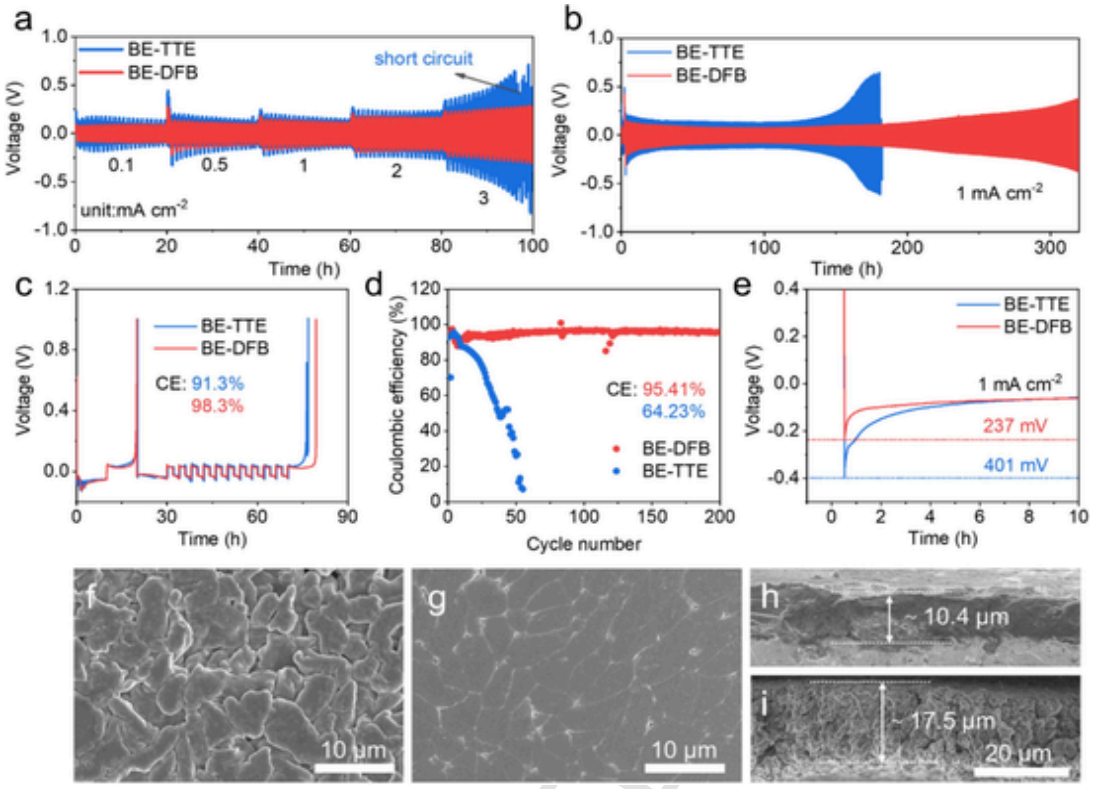

Fig. 4. (a) Rate performance of Li||Li cells using BE-TTE and BE-DFB. (b) Cycling performance of Li||Li cells using BE-TTE and BE-DFB. (c) Aurbach test of Li||Cu cells using BE-TTE and BE-DFB. (d) Cycling performance of Li||Cu cells using BE-TTE and BE-DFB. (e) The nucleation potential of Li||Cu cells with BE-TTE and BE-DFB. (f) SEM image of the electrodeposited Li metal on the Cu foils in BE-TTE. (g) SEM image of the electrodeposited Li metal on the Cu foils in BE-DFB. (h) The cross-section SEM image of the electrodeposited Li metal on the Cu foils in BE-DFB. (i) The cross-section SEM image of the electrodeposited Li metal on the Cu foils in BE-TTE.

mAh g^{-1} and 88.7% capacity retention (Fig. 5e). More significantly, the Fig. 5g shows the 1.8 Ah graphite||NCM811 pouch cells with BE-DFB can achieve a high discharge capacity of 1.41 Ah and 94.5% capacity retention after 200 cycles at −10 °C and 0.5C. On the basis of the results, the properties of diluents were compared in terms of five primary dimensions (Fig. 5f), the DFB presents attractive functionalities outperforming TTE including discharge capacity, cycling performance, price, Li^+ transport and weak solvation ability.

To elucidate the origin of excellent cycling stability of the Li||NCM811 cells using BE-DFB electrolyte, the cycled Li anodes were examined by SEM and X-ray photoelectron spectroscopy (XPS) technology. As revealed in Fig. 6a, the cycled Li anode peeled off from the Li||BE-DFB||NCM811 cells maintains a continuous and intact morphology after cycling at 25 °C, while the surface of Li anodes came from the Li||BE-TTE||NCM811 cells show obvious microcracks and uneven block shaped Li metal (Fig. 6b). Fig. 6c and d shows that the morphology of Li anode after cycling at −20 °C, a loose and dendritic Li structure was observed for Li||BE-TTE||NCM811 cells, in contrast, the Li||BE-DFB||NCM811 cells feature the uniform and nodular Li metal deposition. XPS was used for analyzing the interface components of cycled Li anode. The C 1s spectra mainly conclude R-CO_3, C—O, and C—F for both Li||BE-TTE||NCM811 and Li||BE-DFB||NCM811 cells, which mainly originate from the decomposition of the EC, DEC, and FEC solvents. Similarly, in the F 1s spectra, three peaks are observed at 687.5, 686.6, and 684.8 eV, corresponding to Li_xPF_y, C—F, and LiF, respectively, which are detected by the reduction of PF_6^- anion and FEC solvent (Fig. 6e-h). It is worth noting that there are no distinct peaks attributed to DFB in the F 1s and C 1s spectra, because DFB hardly undergoes oxidation or reduction reactions during the cycling process to participate in the formation of the interfacial layer (Fig. S24 and S25). Upon Ar^+ sputtering of the cycled Li anode of Li||BE-DFB||NCM811 cells, the F 1s signal intensity rapidly increases from 21% to 36%, and the signal of C 1s content rapidly decreases from 39% to 17%. However, only increase of 9% for F 1s content and decrease of 17% for C 1s content were calculated for Li||BE-TTE||NCM811 cells. The SEI films between electrode and electrolyte have obvious organic-inorganic hybrid characteristics. The outer layer is rich in organic components and the inner layer is rich in inorganic components [47]. These results demonstrate that the introduction of weak-field ligand DFB induces the formation of tough SEI with high content of LiF, which help to suppress the formation of Li dendrites during the cycling process. To further demonstrate the superior of SEI formed in BE-DFB electrolyte, the pouch cells with BE and BE-DFB electrolytes were disassembled after charging to 4.3 V at −10 °C. The surface of graphite anode peeled from the graphite||BE-DFB||NCM811 pouch cell is smooth without Li metal plating and presents a golden yellow color, which is attributed to high content of Li on the surface of graphite anode (Fig. S26). While the surface of graphite anode peeled from the graphite||BE ||NCM811 pouch cell has obvious deposition of silver-white Li metal (Fig. 6k,l and S27). The evidences can be supported by SEM image of graphite anodes. The filamentous Li metal deposited on the surface of the graphite anode using BE electrolyte, while the surface of graphite anode using DFB is free of Li dendrites (Fig. 6m,n and S28). In addition, we also evaluated the high-temperature storage performance of graphite||NCM811 pouch cell using different electrolytes, the graphite||NCM811 pouch cell with BE-DFB produced a small amount of gas (Fig. S29b,e), while the graphite||NCM811 pouch cell with BE produced a large amount of gas, causing significant expansion of the cell (Fig. S29c,f). Fig. S30 show

UNCORRECTED

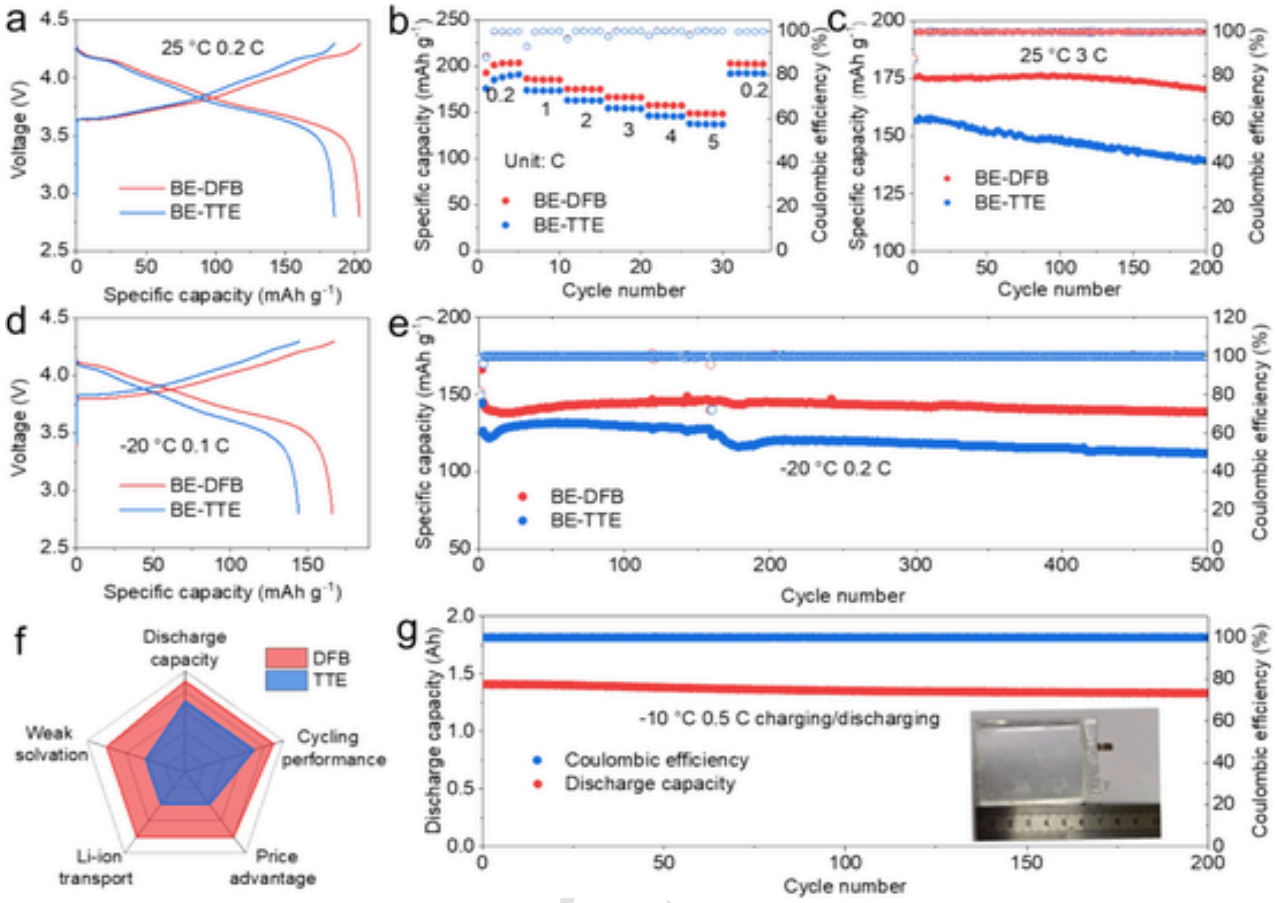

Fig. 5. (a) The charge and discharge curves of Li||NCM811 cells using BE-TTE and BE-DFB at 25 °C and 0.2C. (b) Rate performance of Li||NCM811 cells using BE-TTE and BE-DFB. (c) Cycling performance of Li||NCM811 cells using BE-TTE and BE-DFB at 25 °C and 3C. (d) The charge and discharge curves of Li||NCM811 cells using BE-TTE and BE-DFB at −20 °C and 0.1C. (e) Cycling performance of Li||NCM811 cells using BE-TTE and BE-DFB at −20 °C and 0.2C. (f) Performance comparisons of the TTE and DFB examined in this work based on five operation parameters (discharge capacity, cycling performance, price, Li^+ transport and weak solvation ability). (g) Cycling performance of graphite||NCM811 pouch cell using BE-DFB at −10 °C and 0.5C, the inset is the digital photograph of graphite||NCM811 pouch cell.

that the XRD patterns of cycled NCM811 cathode using BE-DFB and BE-TTE electrolytes. The cycled NCM811 electrode using BE-DFB electrolyte exhibits a slight offset of approximately 0.1°. In the BE-TTE electrolyte, the obvious (003) peak change is a significant positive shift from 18.71° to 18.49° (Fig. S30a). In addition, the intensity ratio of (003)/(104) in cycled NCM622 with BE-TTE and with BE-DFB is 1.30 and 1.59 (Fig. S30b). The results indicate that the introduction of DFB can effectively protect the crystal structure of NCM811 during the long-term cycling.

3. Conclusion

In summary, we have found a weak-field ligand ortho-difluorobenzene diluent to modify the solvation structure of carbonate-based electrolyte based on coordination field theory. Compared with the highly fluorinated diluent TTE, DFB can participate in the coordination of Li^+ to reconstruct soft solvation structure with more cation-anion aggregation, leading to reduce deslovation energy for Li^+ transport and derive LiF-rich SEI. Simultaneously, DFB also acts as an outer solvation sheath mediator to bridge adjacent solvation sheath and establish continuous ion-hopping pathways. Therefore, the 1 M $LiPF_6$ in EC/EMC/DFB (v/v/v = 3/7/10) electrolyte achieves higher ionic conductivity (1.58 mS cm^{-1} vs 1.00 mS cm^{-1} at −20 °C), Li^+ transference number (0.74 vs 0.47), and lower deslovation energy (2.43 eV vs 4.35 eV) than that of the electrolyte with TTE. Li||NCM811 coin cells employing the optimized electrolyte deliver superior electrochemical performance across a wide temperature range. The initial discharge capacity is increased by approximately 20 mAh g^{-1} relative to the TTE, and a high capacity retention of 95.7% is maintained after 500 cycles at −20 °C and 0.2C. Moreover, graphite||NCM811 pouch cells fabricated with the BE-DFB electrolyte retain a high capacity of 1.41 Ah along with 94.5% capacity retention after 200 cycles at −10 °C and 0.5C. These findings establish design principles for weakly coordinating diluents and provide a viable strategy for developing high-performance Li-ion batteries with a wide operating temperature range.

4. Experimental section

See experimental details in the Supporting Information.

CRediT authorship contribution statement

Hao Huang: Writing – original draft, Validation, Methodology, Investigation. **Jingang Zheng:** Methodology, Data curation. **Yiyang Zhao:** Software, Investigation. **Weichen Han:** Software, Conceptualization. **Hongyang Li:** Visualization, Software. **Lixiang Li:** Supervision, Resources. **Hongwei Zhao:** Resources, Funding acquisition. **Han zhang:** Software, Methodology. **Baigang An:** Su-

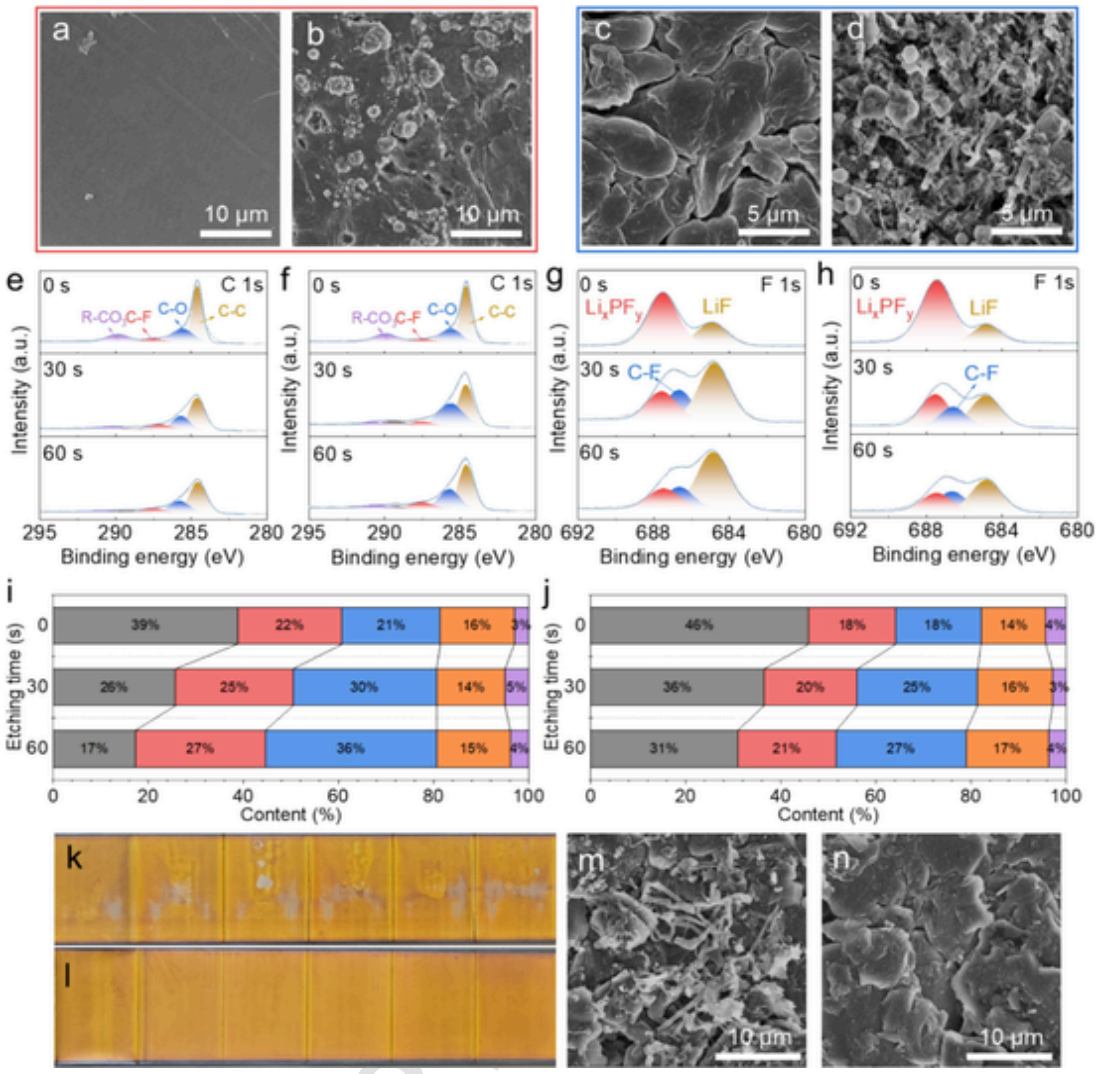

Fig. 6. (a) SEM image of cycled Li anode in BE-DFB at 25 °C. (b) SEM image of cycled Li anode in BE-TTE at 25 °C. (c) SEM image of cycled Li anode in BE-DFB at −20 °C. (d) SEM image of cycled Li anode in BE-TTE at −20 °C. (e) The C 1s spectra of cycled Li anode in BE-DFB at −20 °C. (f) The F 1s spectra of cycled Li anode in BE-DFB at −20 °C. (g) The C 1s spectra of cycled Li anode in BE-TTE at −20 °C. (h) The F 1s spectra of cycled Li anode in BE-TTE at −20 °C. (i) Atomic percentages of elements at varying depths within the SEI formed in BE-DFB. (j) Atomic percentages of elements at varying depths within the SEI formed in BE-TTE, the black squares represent C element, the red squares represent Li element, the blue squares represent F element, the orange squares represent O element, the purple squares represent P element. (k) Digital photograph of graphite peeled from the full-charged graphite||NCM811 with BE. (l) Digital photograph of graphite peeled from the full-charged graphite||NCM811 with BE-DFB. (m) SEM image of graphite peeled from the full-charged graphite||NCM811 with BE. (n) SEM image of graphite peeled from the full-charged graphite||NCM811 with BE-DFB.

pervision, Funding acquisition. **Chengguo Sun:** Writing – review & editing, Supervision, Project administration, Funding acquisition.

Declaration of competing interest

The authors declare that they have no known competing financial interests or personal relationships that could have appeared to influence the work reported in this paper.

Acknowledgements

This work was supported by National Natural Science Foundation of China (22578219 and 52371224), the Fundamental Research Funds for the Liaoning Universities (LJ222410146062, LJ212410146075), the University of Science and Technology Liaoning Talent Project Grants (6003000476).

Data availability

Data will be made available on request.

Appendix A. Supplementary data

Supplementary data to this article can be found online at https://doi.org/10.1016/j.cej.2026.176753.

References

[1] G. Song, Z. Yi, F. Su, L. Xie, Z. Wang, X. Wei, G. Xu, C. Chen, Boosting the low-temperature performance for Li-ion batteries in $LiPF_6$-based local high concentration electrolyte, ACS Energy Lett. 8 (2023) 1336–1343.
[2] Y. Chen, Q. He, Y. Zhao, W. Zhou, P. Xiao, P. Gao, N. Tavajohi, J. Tu, B. Li, X. He, L. Xing, X. Fan, J. Liu, Breaking solvation dominance of ethylene carbonate via molecular charge engineering enables lower temperature battery, Nat. Commun. 14 (2023) 8326.
[3] J. Liu, B. Yuan, N. He, L. Dong, D. Chen, S. Zhong, Y. Ji, J. Han, C. Yng, Y. Liu, W.

UNCORR

He, Reconstruction of LiF-rich interphases through an anti-freezing electrolyte for ultralow-temperature $LiCoO_2$ batteries, Energy Environ. Sci. 16 (2023) 1024–1034.
[4] L. Chen, J. Wang, M. Chen, Z. Pan, Y. Ding, Z. Song, X. Ai, Y. Cao, Z. Chen, "Dragging effect" induced fast desolvation kinetics and −50 °C workable high-safe lithium batteries, Energy Storage Mater. 65 (2024) 103098.
[5] D. Zhao, H. Liang, S. Wu, Y. Quan, X. Hu, J. Li, P. Wang, X. Cui, S. Li, Customizing solid electrolyte interphase with bilayer spatial structure to mitigate swelling towards long-term life lithium battery, J. Energy Chem. 105 (2025) 702–712.
[6] Y. Yao, P. Wang, Y. Zhao, J. Zhang, L. Hu, J. Zhou, Y. Wang, H. Dou, J. Luo, S. Li, D. Zhao, Efficient decomposition of electrolyte salt reconstructing Helmholtz plane for long life sodium-ion batteries, ACS Sustain. Chem. Eng. 13 (2025) 4439–4448.
[7] H. Yu, D. Chen, X. Ni, P. Qing, C. Yan, W. Wei, J. Ma, X. Ji, Y. Chen, L. Chen, Reversible adsorption with oriented arrangement of a zwitterionic additive stabilizes electrodes for ultralong-life Zn-ion batteries, Energy Environ. Sci. 16 (2023) 2684–2695.
[8] W. Liu, Q. Zhao, H. Yu, H. Wang, S. Huang, L. Zhou, W. Wei, Q. Zhang, X. Ji, Y. Chen, L. Chen, Metallic particles-induced surface reconstruction enabling highly durable zinc metal anode, Adv. Funct. Mater. 33 (2023) 2302661.
[9] B. Ma, H. Zhang, R. Li, S. Zhang, L. Chen, T. Zhou, J. Wang, R. Zhang, S. Ding, X. Xiao, T. Deng, L. Chen, X. Fan, Molecular-docking electrolytes enable high-voltage lithium battery chemistries, Nat. Chem. 16 (2024) 1427–1435.
[10] J. Xu, J. Zhang, T. Pollard, Q. Li, S. Tan, S. Hou, H. Wan, F. Chen, H. He, E. Hu, K. Xu, X. Yang, O. Borodin, C. Wang, Electrolyte design for Li-ion batteries under extreme operating conditions, Nature 614 (2023) 694–700.
[11] J. Chen, H. Zhang, M. Fang, C. Ke, S. Liu, J. Wang, Design of localized high-concentration electrolytes via donor number, ACS Energy Lett. 8 (2023) 1723–1734.
[12] P. Zhou, Y. Xiang, K. Liu, Understanding and applying the donor number of electrolytes in lithium metal batteries, Energy Environ. Sci. 17 (2024) 8057–8077.
[13] Q. Li, H. Wang, H. Yu, M. Fu, W. Liu, Q. Zhao, S. Huang, L. Zhou, W. Wei, X. Ji, Y. Chen, L. Chen, Engineering an ultrathin and hydrophobic composite zinc anode with 24 μm thickness for high-performance Zn batteries, Adv. Funct. Mater. 33 (2023) 2303466.
[14] H. Yu, D. Chen, Q. Li, C. Yan, Z. Jiang, L. Zhou, W. Wei, J. Ma, X. Ji, Y. Chen, L. Chen, In situ construction of anode–molecule interface via lone-pair electrons in trace organic molecules additives to achieve stable zinc metal anodes, Adv. Energy Mater. 13 (2023) 2300550.
[15] S. Huang, K. Li, A. Wang, S. He, Z. Xie, H. Li, Z. Wu, Y. Chen, L. Chen, Stable lithium anodes enabled by the hardening and high $Li+$ flux interlayer, Nano Lett. 25 (2025) 9337–9344.
[16] S. Huang, Z. Wu, B. Johannessen, K. Long, P. Qing, P. He, X. Ji, W. Wei, Y. Chen, L. Chen, Interfacial friction enabling ≤ 20 μm thin free-standing lithium strips for lithium metal batteries, Nat. Commun. 14 (2023) 5678.
[17] Z. Yang, C. Wang, Z. Wang, S. He, T. You, A. Wang, Y. Jin, L. Mei, S. Huang, Y. Chen, L. Chen, Fluorocarbon interlayer enhancing fast ion transport for low-temperature lithium metal batteries, J. Colloid Interface Sci. 689 (2025) 137191.
[18] Z. Li, Y. Yao, M. Zheng, S. Sun, Y. Yang, Y. Xiao, L. Xu, C. Jin, X. Yue, T. Song, P. Wu, C. Yan, Q. Zhang, Electrolyte design enables rechargeable $LiFePO_4$/graphite batteries from −80 °C to 80 °C, Angew. Chem. Int. Ed. 137 (2025) e202409409.
[19] Z. Han, L. Chen, G. Zheng, D. Zhang, K. Yang, G. Xiao, H. Xu, Y. Li, X. An, Y. Ma, S. Guo, Y. Chen, T. Hou, Y. Cao, C. Zhang, Y. He, M. Liu, Ionic liquid reinforcing ether coordination of localized high concentration electrolyte enables high-voltage lithium metal batteries, Adv. Mater. 37 (2025) 2416668.
[20] Z. Chen, Z. Zhang, F. Qiu, Z. Gao, H. Xie, Z. Xu, M. Jia, X. Zhang, H. Zhou, Regulating solvation shell to fortify anion-cation coordination for enhanced sodium metal battery stability, ACS Energy Lett. 10 (2025) 177–184.
[21] C. Ha, J.K. Koo, W. To-A-Ran, V.C. Ho, J. Mun, Y.J. Kim, Interfacial control through fluorinated co-solvent electrolytes for enabling uniform Li metal plating and long-term stability in high-voltage lithium metal batteries, Nano Energy 145 (2025) 111445.
[22] X. Lin, X. Wu, S. Son, J. Seminario, P. Balbuena, A. Arboleda, J. Cai, M. Li, Z. Lyu, D. Bresser, R. Amine, C. Sun, K. Amine, Balancing solvation: stabilizing lithium metal batteries via optimized cosolvents for ionic-liquid electrolytes, Energy Environ. Sci. 16 (2025) 7928–7938.
[23] X. Huang, X. Jiang, C. Shi, M. Wang, Y. Zhou, B. Hong, J. Li, Y. Lai, Anion-diluent synergistic strategy for improved interfacial stability in lithium metal batteries, Energy Storage Mater. 78 (2025) 104239.
[24] X. Zhang, T. Yang, Z. Huang, Q. Zhang, S. Jia, J. Kang, C. He, N. Zhao, Y. Zhang, Z. Chen, Fluorinated hybrid diluent modulated electrolyte for wide-temperature 508.5 Wh kg^{-1} lithium metal batteries, ACS Energy Lett. 10 (2025) 4428–4438.
[25] Z. Zhu, Y. Li, J. Ji, X. Qi, J. Pan, J. Ma, L. Qie, Y. Huang, Taming the ion-dipole interaction via rational diluent selection for low-temperature Li-metal batteries, Angew. Chem. Int. Ed. 64 (2025) e202423940.
[26] C. Zhao, Z. Li, B. Chen, F. Chen, C. Wang, Self-adaptive electrolytes for fast-charging batteries, Nat. Energy 10 (2025) 904–913.
[27] J. Li, S. Sui, X. Zhou, K. Lei, Q. Yang, S. Chu, L. Li, Y. Zhao, M. Gu, S. Chou, S. Zheng, Weakly coordinating diluent modulated solvation chemistry for high-performance sodium metal batteries, Angew. Chem. Int. Ed. 63 (2024) e202400406.
[28] C. Wang, K. Wan, P. Liu, C. Zeng, S. Wang, Y. Huang, Y. Zhang, H. Xiao, C. Shu, Z. Liang, Localized high-concentration electrolytes with semi-solvated hexafluoroisopropyl methyl ether diluent for wide-temperature-range lithium metal batteries, Angew. Chem. Int. Ed. 64 (2025) e202506083.
[29] Z. Wang, H. Tu, X. Ma, S. Lu, G. Su, Y. Gao, J. Xue, L. Liu, X. Yao, K. Wang, F. Zhang, Z. Qin, J. Zheng, Q. Wang, J. Xue, L. Chen, H. Li, X. Wu, Flame-retardant electrolytes with electrochemically-inert and weakly coordinating dichloroalkane diluents for practical lithium metal batteries, Nat. Commun. 16 (2025) 10188.
[30] H. Li, S. Li, F. Wang, J. Zhang, A chelating coordination modulation method for the synthesis of Ti-MOF single crystals, Inorg. Chem. Front. 11 (2024) 2876.
[31] F. An, B. Gao, X. Dai, M. Wang, X. Wang, Efficient removal of heavy metal ions from aqueous solution using salicylic acid type chelate adsorbent, J. Hazard. Mater. 192 (2011) 956–962.
[32] J. Liu, Y. Wang, W. Yin, H. Sun, B. Yang, J. Yao, Morphology-tunable anhydrous $MgCO_3$ synthesis from magnesite solid waste via salicylic acid-Na_2EDTA synergistic leaching and carbonation, Chem. Eng. J. 511 (2025) 162168.
[33] D. Lu, R. Li, M. Rahman, P. Yu, L. Lv, S. Yang, Y. Huang, C. Sun, S. Zhang, H. Zhang, J. Zhang, X. Xiao, T. Deng, L. Fang, L. Chen, J. Wang, E. Hu, C. Wang, X. Fan, Ligand-channel-enabled ultrafast Li-ion conduction, Nature 627 (2024) 101–107.
[34] H. Bergstom, B. Mccloskey, Ion transport in (localized) high concentration electrolytes for Li-based batteries, ACS Energy Lett. 9 (2024) 373–380.
[35] X. Dong, Y. Lin, P. Li, Y. Ma, J. Huang, D. Bin, Y. Wang, Y. Qi, Y. Xiao, High-energy rechargeable metallic Lithium battery at −70 °C enabled by a cosolvent electrolyte, Angew. Chem. Int. Ed. Engl. 131 (2019) 5679–5683.
[36] T. Li, X. Zhang, N. Yao, Y. Yao, L. Hou, X. Chen, M. Zhou, J. Huang, Q. Zhang, Stable anion-derived solid electrolyte interphase in lithium metal batteries, Angew. Chem. Int. Ed. Engl. 133 (2021) 22865–22869.
[37] C. Li, Y. Li, Y. Wang, F. Bai, X. Chen, T. Li, Developing diluted low-concentration electrolyte with a high anion-to-solvent ratio for high-voltage Lithium metal batteries, J. Mater. Chem. A 12 (2024) 8236–8243.
[38] Y. Wu, Q. Hu, H. Liang, A. Wang, H. Xu, L. Wang, X. He, Electrostatic potential as solvent descriptor to enable rational electrolyte design for Lithium batteries, Adv. Energy Mater. 13 (2023) 2300259.
[39] Y. Li, D. Dong, J. Huang, F. Zeng, W. Liang, Z. Xie, L. Quan, C. Chen, Y. Liao, D. Bedrov, L. Xing, W. Li, A miss is as good as a mile: prediction of additive effectiveness in sodium-ion batteries based on electrostatic potential, ACS Energy Lett. 10 (2025) 2564–2573.
[40] L. Chen, X. He, Y. Chen, Y. Hou, Y. Zhang, K. Wang, X. Ai, Y. Cao, Z. Chen, Manipulating interfacial stability via preferential absorption for highly stable and safe 4.6 V $LiCoO_2$ cathode, Nano Micro Lett. 17 (2025) 181.
[41] P. Xiao, Y. Zhao, Z. Piao, B. Li, G. Zhou, H. Cheng, A nonflammable electrolyte for ultrahigh-voltage (4.8 V-class) Li||NCM811 cells with a wide temperature range of 100 °C, Energy Environ. Sci. 15 (2022) 2435–2444.
[42] C. Wang, Z. Sun, Y. Liu, L. Liu, X. Yin, Q. Hou, J. Fan, J. Yan, R. Yuan, M. Zheng, Q. Dong, A weakly coordinating-intervention strategy for modulating Na^+ solvation sheathes and constructing robust interphase in sodium-metal batteries, Nat. Commun. 15 (2024) 6292.
[43] G. Li, V. Koverga, A. Nguyen, R. Kou, M. Ncube, H. Jiang, K. Wang, M. Liao, H. Guo, J. Chen, N. Dandu, A. Ngo, D. Wang, Enhancing lithium-metal battery longevity through minimized coordinating diluent, Nat. Energy 9 (2024) 817–827.
[44] G. Li, X. Lyu, A. Nguyen, R. Kou, C. George, S. Wu, R. Li, K. Wang, T. Li, D. Wang, Fine-tuning Li-ion solvation structure by enhanced solvent-diluent interactions for long-cycling lithium metal batteries, Adv. Energy Mater. 15 (2025) 2405680.
[45] C. Xiao, P. Wen, F. Luo, D. Yu, H. Wang, Z. Zhou, W. Li, X. Zhang, X. Lin, Ultrahigh-voltage lithium metal batteries enabled by single-ion and weakly-solvating nanometric aggregates, Angew. Chem. Int. Ed. 64 (2025) e202502465.
[46] Q. Li, G. Liu, Y. Chen, J. Wang, P. Kumar, H. Xie, W. Wahyudi, H. Yu, Z. Wang, Z. Ma, J. Ming, Electrolyte solvent-ion configuration deciphering lithium plating/stripping chemistry for high-performance lithium metal battery, Adv. Funct. Mater. 35 (2025) 2420327.
[47] J. Zhang, H. Zhang, S. Wen, R. Li, D. Lu, T. Deng, S. Zhang, L. Lv, J. Qi, X. Xiao, L. Fan, S. Geng, F. Wang, L. Chen, M. Noked, X. Wang, X. Fan, Multifunctional solvent molecule design enables high-voltage Li-ion batteries, Nat. Commun. 14 (2023) 2211.

UNCORRECTED PROOF